ARTICLES SCIENCE CHINA Materials

mater.scichina.com link.springer.com

Published online 2 April 2020 | https://doi.org/10.1007/s40843-019-1263-1
Sci China Mater 2020, 63(11): 2206–2214

SPECIAL TOPIC: Advanced Photocatalytic Materials

Tungsten bronze $Cs_{0.33}WO_3$ nanorods modified by molybdenum for improved photocatalytic CO_2 reduction directly from air

Lian Yi, Wenhui Zhao, Yanhong Huang, Xiaoyong Wu*, Jinlong Wang* and Gaoke Zhang

ABSTRACT **Photocatalytic CO_2 reduction is thought to be a promising strategy in mitigating the energy crisis and several other environmental problems. Hence, modifying or developing suitable semiconductors with high efficiency of photocatalytic CO_2 reduction property has become a topic of interest to scientists. In this study, a series of Mo-modified $Cs_{0.33}WO_3$ tungsten bronze were prepared using a "water-controllable releasing" solvothermal method to produce effective photocatalytic CO_2 reduction performance. Interestingly, Mo atoms replaced W partially within the hexagonal crystal structure, leading to a significant increase in photocatalytic CO_2 reduction activity of $Cs_{0.33}WO_3$. The 5% Mo-doped compound displayed the best performance, with the production yield rates of 7.5 μmol g^{-1} h^{-1} for CO and 3.0 μmol g^{-1} h^{-1} for CH_3OH under low concentration of CO_2 under anaerobic conditions, which is greatly higher than those of pure $Cs_{0.33}WO_3$ (3.2 μmol g^{-1} h^{-1} for CO and 1.2 μmol g^{-1} h^{-1} for CH_3OH) and Mo-doped $W_{18}O_{49}$ (1.5 μmol g^{-1} h^{-1} for CO and 0 μmol g^{-1} h^{-1} for CH_3OH). More importantly, the as-prepared Mo-doped $Cs_{0.33}WO_3$ series could also induce the photocatalytic reduction of CO_2 directly from the air in the presence of oxygen, which is beneficial for practical applications. The superior photocatalytic performance of Mo-doped $Cs_{0.33}WO_3$ series over the popular reduced WO_3 may be due to the increase in light absorption induced by the localized surface plasmon resonance (LSPR) effect of Mo^{5+}, large improved charge separation ability, and the co-effect of Mo and Cs in crystal. This study provides a simple strategy for designing highly efficient photocatalysts in low concentration of CO_2 reduction.**

Keywords: CO_2 reduction, charge separation, $Cs_{0.33}WO_3$, low concentration, photocatalytic performance

INTRODUCTION

Over the past few decades, our consumption of fossil fuel has grown significantly, playing an essential role in the development of industrial economy. However, the over-consumption of fossil fuels has led to resource depletion and increasing atmospheric CO_2 concentration, destabilizing the natural carbon cycle [1]. From the 1970s until now, atmospheric CO_2 concentration increased from 280 ppm to ca. 410 ppm, leading to severe global environmental issues such as climate change [2]. Capturing and converting atmospheric CO_2 as a renewable fuel source is a promising strategy to mitigate the current global energy crisis and simultaneously reduce the adverse effects of greenhouse gas (GHG) accumulation in our atmosphere [3,4]. Photocatalytic CO_2 reduction can potentially be used as a method to achieve the above objective. Under sustained solar irradiation, photocatalysts can reduce CO_2 into value-added products, such as CO, HCOOH, HCHO, CH_3OH, and CH_4, which can be further used as industrial raw materials and fuels [5–8]. Nevertheless, atmospheric CO_2 is very stable and requires a high energetic input (>750 kJ mol^{-1}) to break the C=O bond during the reduction reaction [9,10]. Furthermore, H_2 gas is produced during the CO_2 reduction process, which is potentially problematic as H^+ reduction is theoretically more favorable than CO_2 reduction [11,12]. Hence, to overcome the two above obstacles, developing a suitable photocatalyst with good CO_2 activation and poor H_2 reduction ability is essential to increase the efficiency of the CO_2 reduction reaction.

Recently, the photocatalyst WO_3 has attracted increasing attention from researchers studying CO_2 reduction. Given its relatively narrow bandgap (2.4–2.8 eV), stable

School of Resources and Environmental Engineering, Wuhan University of Technology, Wuhan 430070, China
* Corresponding authors (emails: parawu521@163.com (Wu X); wjl16@whut.edu.cn (Wang J))

chemical properties, CO_2 adsorption ability, and relatively low conduction band position, WO_3 prevents the build-up of H_2 during the CO_2 reduction reaction [13–17]. However, the photocatalytic CO_2 reduction activity of WO_3 is still low, due to the poor reductive capacity of the conduction band, the high-charge recombination and the limited number of active sites available for CO_2 activation [18,19]. To improve the photocatalytic performance of materials, scientists have started to use heterojunction [20–23]. Shi *et al.* [24] reported that the photocatalytic CO_2 reduction ability of WO_3 nanosheets was significantly increased after coupling with Cu_2O to form a Z-scheme heterojuction, due to the promoted charge separation and increased redox ability. Furthermore, researchers have found that the introduction of oxygen vacancies and reduced W^{5+} in WO_3 can also significantly improve its photocatalytic CO_2 reduction activity. The creation of oxygen vacancies and W^{5+} in WO_3 increases the surface negative charge density and the number of active sites, which in turn increases CO_2 adsorption and activation [18,25,26]. For example, Xi *et al.* [27] prepared ultrathin $W_{18}O_{49}$ nanowires to investigate their photocatalytic CO_2 reduction property. They showed that the catalytic performance of $W_{18}O_{49}$ with abundant oxygen vacancies and W^{5+} was much higher than that of WO_3 alone, which can be attributed to the enhanced light absorption, increased number of active sites, and decreased CO_2 activation energy. Moreover, the studies [28–30] also revealed that doping Mo in oxygen vacancy-rich WO_3 could further improve its photocatalytic performance. The addition of Mo to oxygen vacancy-rich WO_3 can not only generate more oxygen vacancies, W^{5+}, and active sites, but also benefit for the CO_2 activation [28–30]. More interestingly, our groups recently unveiled that incorporating alkali metal ions into reduced WO_3 formed unique hexagonal tungsten bronze ($M_{0.33}WO_3$, M=K, Rb, Cs), in which the alkali metal ions were found at the hexagonal tunnel of crystal and formed weak chemical bonds with W and O. Taking advantage of this peculiar structure, $M_{0.33}WO_3$ showed an outstanding photocatalytic CO_2 reduction activity, much higher than $W_{18}O_{49}$ and WO_3 [31]. This superiority stems from the enhanced light absorption, the additional number of active sites, reduced charge recombination, and CO_2 activation energy [31]. Based on the above research, adding more Mo into $M_{0.33}WO_3$ crystals is predicted to significantly improve its photocatalytic CO_2 reduction performance compared with solely alkali metals and Mo-induced counterparts. However, this prediction has not yet been verified by empirical research, nor have its practical applications been thoroughly investigated.

In this study, series of Mo-modified $Cs_{0.33}WO_3$ hexagonal tungsten bronze were successfully prepared using a "water-controllable releasing" solvothermal method, to investigate its photocatalytic CO_2 reduction property in normal conditions and under low atmospheric CO_2 concentration. Interestingly, doping $Cs_{0.33}WO_3$ with Mo was found to further enhance its photocatalytic ability. As expected, under full spectrum Xe irradiation, Mo-modified $Cs_{0.33}WO_3$ series showed excellent photocatalytic CO_2 reduction activity, much higher than that of $Cs_{0.33}WO_3$ and Mo-doped $W_{18}O_{49}$. The charge separation ability of the samples was studied by photoluminescence spectra and photoelectrochemical test. Finally, a possible photocatalytic CO_2 reduction process over Mo-doped $Cs_{0.33}WO_3$ was proposed based on *in-situ* fourier transform infrared reflection (FTIR) spectra.

EXPERIMENTAL SECTION

Materials

All reagents were of analytical grade, purchased from Sinopharm Chemical Reagent Co. Ltd. and used without further treatment.

Preparation of Mo-modified $Cs_{0.33}WO_3$ series

The typical preparation process was as follows: 0.3 g of WCl_6 was dissolved in 40 mL of ethanol. Then, the fixed amounts of $MoCl_5$ (0, 6.2, 10.33 and 20.67 mg) were added to the solution and stirred vigorously for 30 min. Next, 0.067 g of $CsOH{\cdot}H_2O$ and 10 mL of acetic acid were added and stirred vigorously for another 30 min. The mixed solution was then transferred into a 100 mL-Teflon vessel and heat-treated at 220°C for 20 h. After being cooled down to room temperature, the particles were centrifuged, washed and dried in a vacuum oven overnight. The samples with various $MoCl_5$ additions (0, 6.2, 10.33 and 20.67 mg) were designated as CsWO, 3% Mo-CsWO, 5% Mo-CsWO, and 10% Mo-CsWO, respectively. The percentages (3%, 5%, 10%) indicate the molar ratios of Mo/W in the samples. The control Mo-doped $W_{18}O_{49}$ was prepared in the same way, but without the addition of $CsOH{\cdot}H_2O$.

Characterizations

Sample crystallinity was recorded by X-ray diffraction (XRD) patterns using Cu-Kα radiation (D/MAX-RB). The morphologies and structures of the samples were measured using transmission electron microscopy (TEM), high-resolution TEM (HRTEM) and element

mapping (JEM2100F). The surface states of atoms in the sample were collected using X-ray photoelectron spectroscopy (XPS) (ESCALAB II) and the corresponding binding energy positions of the atoms were calibrated according to 284.5 eV of C 1s. The light absorption of the samples was plotted by UV-2550 (Shimadzu, Japan). The photoluminescence (PL) spectra of the products were obtained using a fluorescence spectrophotometer (RF-5301PC). The *in-situ* FTIR spectra of the samples were conducted using a Bruke Tensor II FTIR spectrometer. The photoelectrochemical properties of the samples were checked by a common three-electrode system (CHI-660E). Pt and Ag/AgCl were separately used as counter and reference electrodes [32,33].

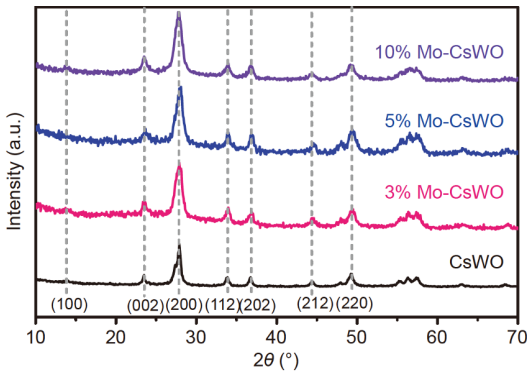

Figure 1 XRD patterns of CsWO and Mo-doped samples with various concentrations.

Photocatalytic CO_2 reduction test

The photocatalytic CO_2 reduction activity of the prepared samples was evaluated in a 500-mL home-made glass vessel. First, 50 mg of sample particles were uniformly dispersed in a Petri dish by ultrasonication and drying, then put at the bottom of a glass vessel. In this reactor, the fresh air was used as a CO_2 reduction atmosphere and 500 μL of deionized water was also injected. After the 300 W Xe lamp (850 mW cm^{-2}) was turned on, 200 μL of gas were withdrawn to identify the products using gas chromatography (GC) (7820, Zhongkehuifen China) at determined time intervals.

The low concentration of CO_2 (ca. 1000 ppm) reduction under anaerobic conditions was produced by reacting concentrated H_2SO_4 with $NaHCO_3$ in an N_2 atmosphere instead of fresh air. The other procedures were the same as those of fresh air condition.

RESULTS AND DISCUSSION

As shown in Fig. 1, the diffraction peaks of CsWO are consistent with the pure hexagonal tungsten bronze phase (JCPSD No. 831334) and no other impurities can be observed. The peaks located at 14.2°, 23.5°, 27.5°, 34.1°, 36.4°, 44.8°, and 49.7° can be assigned to the crystal planes of (100), (002), (200), (112), (202), (212) and (220) in CsWO, respectively. Furthermore, the peak at (200) exhibited the strongest intensity compared with the other peaks, indicating that the CsWO crystal preferentially grows in the [100] direction. When Mo-doped CsWO was used, all the samples showed similar patterns as CsWO and no other big difference was observed, possibly because Mo and W have similar ionic radii, meaning that doping with Mo did not change the structure of the tungsten bronze.

To investigate the shapes and structures of the synthesized particles, TEM, HTREM, and element mapping analysis were carried out, the results of which are presented in Fig. 2. The sample displayed the nanorod morphology and clear crystal plane fringes with the d-spacing of 0.32 nm (Fig. 2a and b), which is well-indexed to the (300) planes of CsWO. This means that the sample crystal preferentially grew along the [100] axis, similarly to the XRD results as presented above. From the element mapping (Fig. 2c–g), the elements Mo, Cs, W, and O all appear uniformly dispersed in the nanorods. Therefore, the above results could confirm that the particles prepared in this study were hexagonal tungsten bronze $Cs_{0.33}WO_3$ and Mo was successfully inserted into CsWO

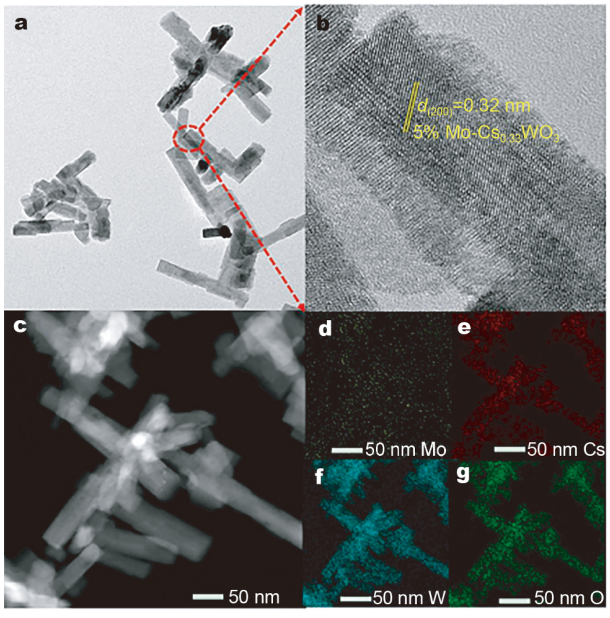

Figure 2 TEM (a), HRTEM (b) and element mapping (c–g) images of the sample 5% Mo-CsWO.

crystals.

The surface states of atoms in CsWO were studied by XPS spectra, as shown in Fig. 3. Fig. 3a presents the survey spectra of the samples, showing that the sample atoms were all exhibited in the spectra, consistently with the element mapping results. The high-resolution XPS spectra of W 4f over samples could be fitted into two pairs of peaks. The large pair of peaks located at ca. 37.7 and 35.6 eV could be attributed to the binding energies of W^{6+}, while the small pair of peaks situated at ca. 36.8 and 34.7 eV should be ascribed to the corresponding energies of W^{5+} [34]. These results show that within the CsWO crystal, tungsten was mainly found as W^{6+} and partially as W^{5+}, produced by the reduction of ethanol in the solvothermal reaction of raw materials and very essential for the near infrared (NIR) light absorption of CsWO [35,36]. In the relevant O 1s spectra, the lines could be deconvoluted into two main peaks at 530.5 and 531.4 eV, caused by the binding energies of the lattice oxygen in CsWO and surface OH groups, respectively. As for Mo doped CsWO, its 3d XPS spectra also could be revealed by two groups of peaks. The lower energies of the paired peaks located at 229.1 and 234.2 eV were owing to the Mo^{5+}, while the higher ones situated at 232.8 and 235.9 eV originated from the Mo^{6+}. This suggests that Mo was present in the crystal, with multi-valence replacing W positions. Additionally, according to the inductively coupled plasma (ICP) measurement and XPS analysis, the molar ratios of Mo/W in the 5% Mo-CsWO sample were reported as 4.32% and 4.64%, respectively. The figures are close to the theoretical values and further confirm that Mo exists within the CsWO crystal. Furthermore, electron paramagnetic resonance (EPR) analysis was used to prove the existence of oxygen vacancy in the samples. From the results in Fig. S1 (Supplementary information), no obvious signals at g=2.001 (indicating the presence of oxygen vacancy) can be detected in the EPR spectra of either sample. Therefore, there is no hard evidence for the existence of oxygen vacancies in CsWO series, similarly to the results from previous research [28,30,31]. While for the Mo-doped CsWO sample, the strong signals with parallel ($g_{//}$=1.846) and perpendicular ($g_{\perp}$=1.907) bands were demonstrated, which should be due to the unsaturated coordination of Mo^{5+} and beneficial for CO_2 activation [28,30].

The optical property and band structure information of each sample are shown in Fig. 4. From Fig. 4a, it is explicit that all samples exhibit light absorption in the UV and partially-visible light ranges, which should be due to the intrinsic band absorption of CsWO. Interestingly, they also presented very strong NIR light from 680 to 2500 nm. This strong absorption may result from the

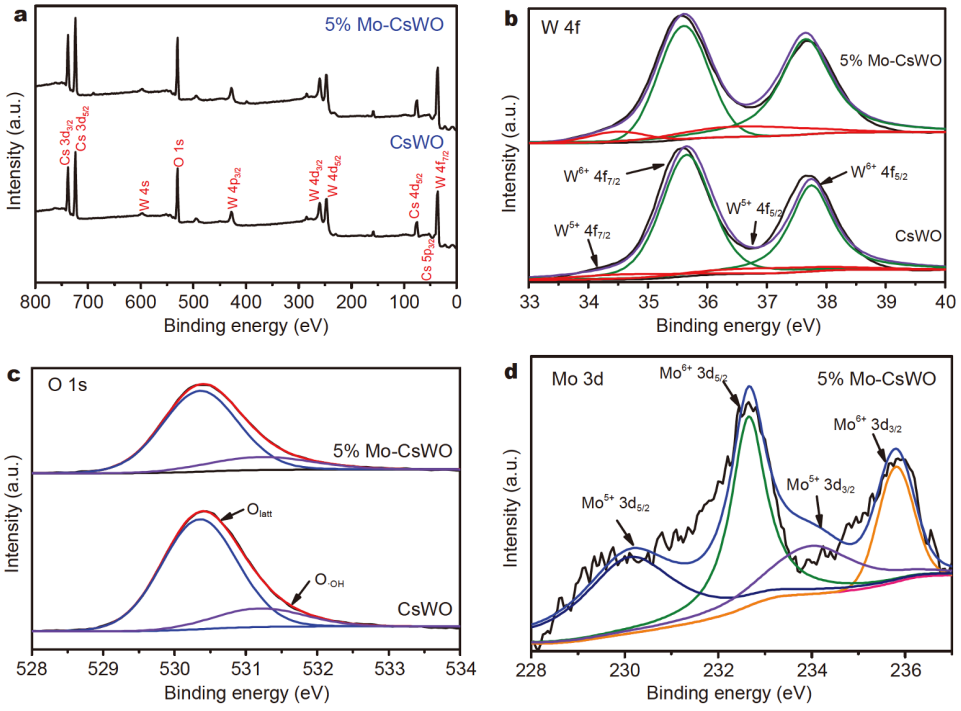

Figure 3 XPS spectra of the samples CsWO and 5% Mo-CsWO: (a) survey, (b) Cs 3d, (c) W 4f, (d) O 1s, and (e) Mo 3d.

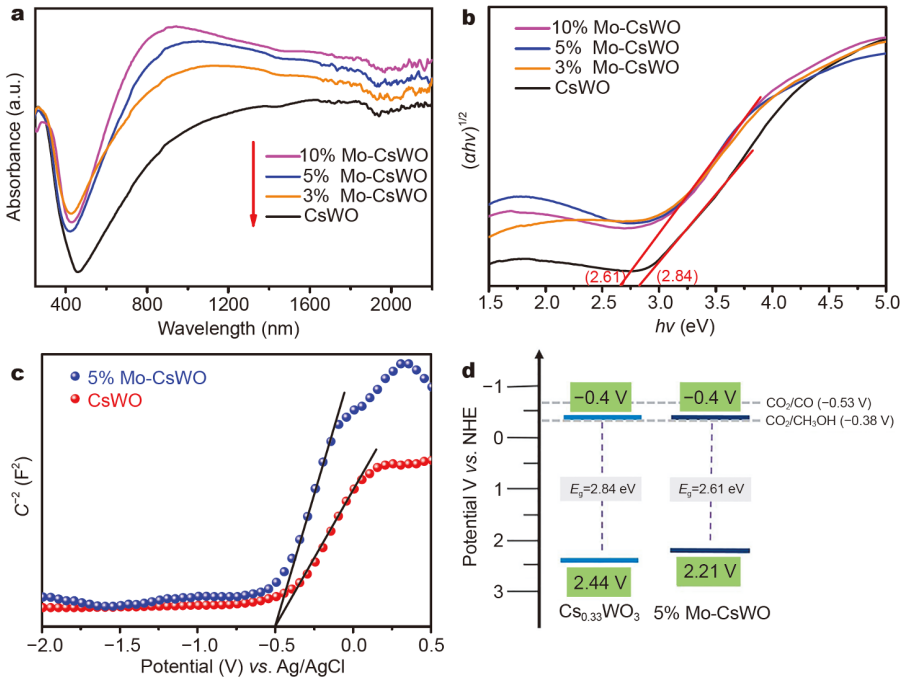

Figure 4 Diffuse reflectance spectroscopy (a) and the corresponding Tauc plots (b) of the prepared four samples, and the Mott-Schottky lines (c) and the proposed band structures (d) for the CsWO and 5% Mo-CsWO samples based on calculations.

localized surface plasmon resonance (LSPR) and polarons effects induced by the presence of reduced W^{5+} in CsWO crystal [25,31,35]. Furthermore, with increasing Mo-doping in CsWO, the NIR absorption ability of the samples also increased, given that in addition to W^{5+}, some Mo^{5+} was also induced in the CsWO crystal, which could produce an LSPR effect as that of W^{5+} to further increase the NIR light absorption [37]. From the lines illustrated in Fig. 4b, it can be inferred that the bandgap of CsWO is about 2.61 eV, while as Mo is incorporated, the bandgaps of the samples shift to lower energies (about 2.84 eV for 5% Mo-doped specimen). Similar results were observed in previous research [28,30]. To figure out the samples' bandgap structure, an electrochemical Mott-Schottky examination was performed, as shown in Fig. 4c. Both samples of CsWO and 5% Mo-CsWO exhibited positive slopes (corresponding to n-type semiconductors) and intercepted the same flat potential with about −0.5 V (*vs.* Ag/AgCl). It is well known that the conduction band (CB) position of semiconductors should be ca. 0.1 V upon the flat potential over n-type semiconductors. After referring the Ag/AgCl potential to a normal hydrogen electrode, the CB position of the samples could be obtained as −0.4 V for both samples. Based on the results shown in Fig. 4b and c, the valence band (VB) positions could be calculated as 2.44 and 2.21 V for CsWO and 5% Mo-CsWO, respectively. The corresponding band structure diagrams of these two samples are illustrated in Fig. 4d. It is obvious that after Mo doping into the CsWO crystal, the CB position of the semiconductor was not changed but the VB position was moved into lower energy. Furthermore, the CB positions of the two samples were higher than that of the CO_2/CH_3OH redox potential but lower than that of the CO_2/CO redox potential, indicating that under suitable light irradiation, these two samples can reduce CO_2 into CH_3OH, but not into CO, at least in theory. However, under some special circumstances, such as the presence of reduced W^{5+} and other defects in the particle surface, CO_2 can be reduced to CO below the potential of −0.53 V as the activation energy of CO_2 reduction to CO decreases in the presence of specific ions and defects [23,24,26,31].

In this study, the samples' photocatalytic activities were evaluated through CO_2 reduction under the full spectrum of 300 W Xe lamp. Interestingly, the photocatalytic reaction worked under both anaerobic low CO_2 and normal atmospheric conditions. Since tungsten bronze is an efficient photo-to-thermal conversion material [38], the surface temperature of the catalyst should be considered under light irradiation, as it probably impacts photocatalytic activity. In this study, the surface temperature of the catalyst was ca. 60°C under Xe illumination, which

allowed the generation of H_2O vapor, creating a favorable environment for the photocatalytic reaction. More detailed information about the effect of temperature on the photocatalytic CO_2 reduction has been investigated in a previous study [31]. Fig. 5a and b present the CO and CH_3OH yields from a low concentration of CO_2 reduction under anaerobic conditions over various samples. It can be observed that, under full Xe irradiation, pure CsWO produced ca. 15 μmol g^{-1} of CO and 4 μmol g^{-1} of CH_3OH during 4 h, while for Mo-doped $W_{18}O_{49}$, only ca. 7 μmol g^{-1} of CO and negligible amounts of CH_3OH were produced, indicating that Cs doping in reduced WO_3 is more active for photocatalytic CO_2 reduction than that of Mo doping one. Interestingly, as Mo doped into CsWO, the photocatalytic activity significantly improved compared with those of solely Cs and Mo-doped WO_3 compounds. When Mo doping concentration was 5% in CsWO, the sample showed the highest photocatalytic activity with ca. 30 μmol g^{-1} of CO and 12 μmol g^{-1} of CH_3OH yields. Further increasing Mo doping to 10%, the activity decreased, probably as too much Mo doping would make some of Mo sites become a trapping center and detrimental for charge separation. To further examine their practical applications, Fig. 5c exhibits the photocatalytic CO_2 reduction performances of the prepared samples directly from the air in the presence of O_2. Intriguingly, the CsWO and Mo-doped CsWO samples all showed observable photocatalytic activity, implying that the presence of O_2 did not negatively contribute to CO_2 reduction in this study. Similarly, the 5% Mo-CsWO also presented the optimal photocatalytic reduction ability with the yield rates of ca. 3.4 μmol g^{-1} h^{-1} for CO and ca. 1 μmol g^{-1} h^{-1} for CH_3OH. Fig. 5d shows the photocatalytic CO_2 reduction performance of 5% Mo-CsWO under various conditions. Under dark conditions or without a catalyst, no obvious activity was observed, but in their presence, the sample displayed the apparent photocatalytic CO_2 reduction performance and the activity in the anaerobic status was twice higher than that under fresh air. Meanwhile, under a pure N_2 atmosphere, the trace of products was examined, due to the existence of small amounts of carbon-related organic materials on the surface of the sample after the solvothermal reaction. The above results showed that the co-incorporation of Mo and Cs in reduced WO_3 was effective at improving photocatalytic CO_2 reduction performance compared with solely modified ones. More importantly, the developed samples were able to effectively reduce CO_2 directly from the air in the presence of O_2 rather than in the commonly-used anaerobic atmosphere. It is well known that the reduction potential of O_2 (+0.82 V) is much higher than that of CO_2, suggesting that, in normal atmospheric conditions O_2 should be reduced before CO_2. However, in this study, O_2 did not negatively contribute to CO_2 reduction. This unexpected result maybe because the CsWO series preferentially adsorbed CO_2 on the

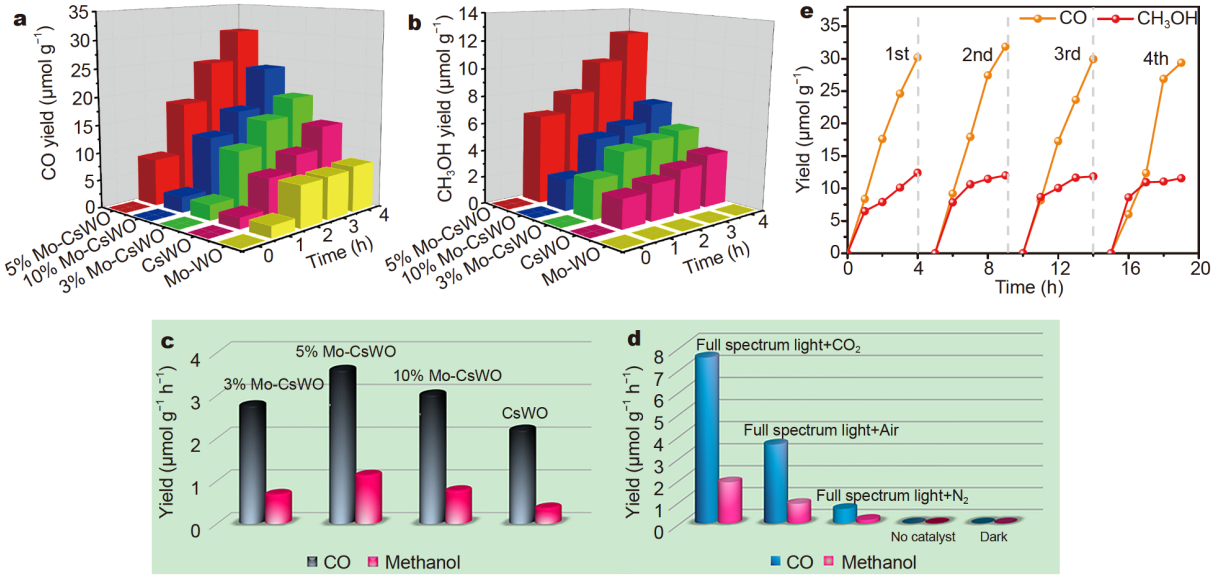

Figure 5 CO (a) and CH_3OH (b) yields from the anaerobic CO_2 reduction during 4 h irradiation, and the corresponding productions with reaction rates from fresh air reduction (c) over the as-prepared samples; photocatalytic CO_2 reduction rate as a function of various conditions (d) as well as photocatalytic stability (e) of the sample 5% Mo-CsWO.

surface but rarely adsorbed O_2 from the atmosphere, such that O_2 reduction was negligible compared with that of CO_2 on the catalyst surface. Detailed information on this process can be accessed from our previous work [31].

As illustrated in Fig. 5e, after four tests, the 5% Mo-CsWO sample still showed relatively good photocatalytic stability, with only about 5% decrement. Meanwhile, the corresponding structure and chemical composition of the catalyst after the catalytic cycles were analyzed using XRD and XPS, as shown in Figs S2 and S3. It is apparent that after the photocatalytic reaction, no significant difference was observed in the structure, surface property, and composition of the sample compared with the fresh sample without photocatalytic reaction, indicating that the Mo-CsWO also has good structural stability.

To unveil the mechanism leading to the superior photocatalytic performance of the Mo-CsWO series, PL spectra and photoelectrochemical tests were conducted, the results of which are illustrated in Fig. 6a–c. It can be seen from Fig. 6a that under irradiation at 312 nm, all samples showed an emission peak and 5% Mo-CsWO exhibited the lowest emission intensity, indicating that this sample had the best charge separation ability compared with the other samples [39]. Similar results were also revealed in photoelectrochemical characterization, where 5% Mo-CsWO showed the highest photocurrent signals and the lowest resistance ability among the samples, suggesting that photogenerated electrons in 5% Mo-CsWO could transfer faster and accumulate on the surface to produce photocatalysis. Hence, based on the above findings, the superiority of photocatalytic CO_2 reduction ability in Mo-CsWO series is thought to be mainly due to its enhanced light-harvesting capacity, as well as its improved charge transfer and separation ability. To explore the CO_2 reduction process, *in-situ* FTIR analysis was carried out under different conditions, as shown in Fig. 6d. Before the light was turned on in the presence of the catalysts (CO_2 and/or water), the surface of the Mo-CsWO samples presented several groups of peaks with weak intensities. Peaks located at around 2300 and 3720 cm^{-1} should be assigned to the adsorbed levels of CO_2 and H_2O. Interestingly, as the light was turned on, the relative intensities of these two groups increased significantly, indicating light irradiation is beneficial for CO_2 and H_2O adsorption on the catalyst surface and subsequently increases CO_2 reduction. Furthermore, one group of peaks in the range of 1300–1600 cm^{-1} (mainly ascribed to the carbonate-related groups and CO) also gradually appeared with light irradiation. After the light was turned off, however, these peaks weakened, suggesting that the photocatalytic CO_2 reduction occurred on the surface of Mo-CsWO. Therefore, when considering the

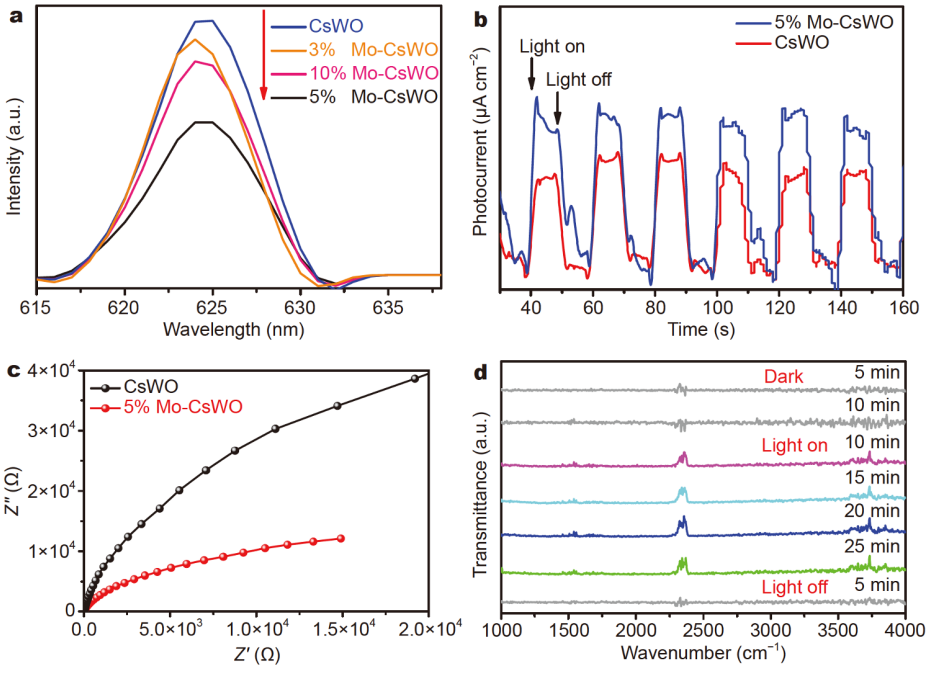

Figure 6 PL spectra (a), transient photocurrent response lines (b) and electrochemical impedance plots (c) of the samples, and the *in-situ* FTIR spectra (d) of the sample 5% Mo-CsWO during the CO_2 reduction.

in-situ FTIR results, the photocatalytic CO_2 reduction reaction was proposed as follows. First, CO_2 and H_2O vapor are gradually adsorbed on the surface of Mo-CsWO particles. Under the light irradiation, H_2O reacts to form hydroxyl groups and CO_2 is activated into carbonate groups. Gradually, the activated H_2O and CO_2 each react to produce $COOH^*$, which plays an essential role in the photoreduction of CO_2 into CO. Next, $COOH^*$ species are protonated further into CO^* molecules and CH_3OH^* through multiple processes. Finally, the CO^* and CH_3OH^* species on the catalyst surface desorb to produce the final products.

CONCLUSIONS

In this study, a series of Mo-doped CsWO were successfully prepared using a special solvothermal method. The resulting sample was a unique hexagonal tungsten bronze, with Mo uniformly but only partially replacing the W positions in the crystal. After Mo doping, the bandgap of CsWO was slightly narrowed, which increased its light absorption capacity through the induction of reduced Mo^{5+}, causing the LSPR effect Interestingly, Mo-doped CsWO showed excellent photocatalytic CO_2 reduction ability under both aerobic and anaerobic conditions, which was significantly higher compared with those of Cs-doped WO_3 and Mo-doped $W_{18}O_{49}$. This difference is most likely due to the enhanced light-harvesting capacity, as well as higher charge separation and transfer. This study provides a simple strategy to improve the photocatalytic performance toward low-concentration CO_2 reduction.

Received 24 December 2019; accepted 31 January 2020; published online 2 April 2020

1 Xiong J, Song P, Di J, *et al.* Ultrathin structured photocatalysts: A versatile platform for CO_2 reduction. Appl Catal B-Environ, 2019, 256: 117788
2 Wu HL, Li XB, Tung CH, *et al.* Semiconductor quantum dots: An emerging candidate for CO_2 photoreduction. Adv Mater, 2019, 31: 1900709
3 Li H, Liu X, Chen S, *et al.* Edge-exposed molybdenum disulfide with N-doped carbon hybridization: A hierarchical hollow electrocatalyst for carbon dioxide reduction. Adv Energy Mater, 2019, 9: 1900072
4 Liu J, Shi W, Ni B, *et al.* Incorporation of clusters within inorganic materials through their addition during nucleation steps. Nat Chem, 2019, 11: 839–845
5 Tang Y, Zhou P, Chao Y, *et al.* Face-to-face engineering of ultrathin Pd nanosheets on amorphous carbon nitride for efficient photocatalytic hydrogen production. Sci China Mater, 2019, 62: 351–358
6 Zhang N, Long R, Gao C, *et al.* Recent progress on advanced design for photoelectrochemical reduction of CO_2 to fuels. Sci China Mater, 2018, 61: 771–805
7 Yang D, Wang G, Wang X. Photo- and thermo-coupled electrocatalysis in carbon dioxide and methane conversion. Sci China Mater, 2019, 62: 1369–1373
8 Han C, Li J, Ma Z, *et al.* Black phosphorus quantum dot/g-C_3N_4 composites for enhanced CO_2 photoreduction to CO. Sci China Mater, 2018, 61: 1159–1166
9 Bie C, Zhu B, Xu F, *et al. In situ* grown monolayer N-doped graphene on CdS hollow spheres with seamless contact for photocatalytic CO_2 reduction. Adv Mater, 2019, 31: 1902868
10 Low J, Dai B, Tong T, *et al. In situ* irradiated X-ray photoelectron spectroscopy investigation on a direct Z-scheme TiO_2/CdS composite film photocatalyst. Adv Mater, 2019, 31: 1802981
11 Li X, Yu J, Jaroniec M, *et al.* Cocatalysts for selective photoreduction of CO_2 into solar fuels. Chem Rev, 2019, 119: 3962–4179
12 Xia P, Antonietti M, Zhu B, *et al.* Designing defective crystalline carbon nitride to enable selective CO_2 photoreduction in the gas phase. Adv Funct Mater, 2019, 29: 1900093
13 Jiang Z, Sun W, Miao W, *et al.* Living atomically dispersed Cu ultrathin TiO_2 nanosheet CO_2 reduction photocatalyst. Adv Sci, 2019, 6: 1900289
14 Li J, Yan P, Li K, *et al.* Cu supported on polymeric carbon nitride for selective CO_2 reduction into CH_4: A combined kinetics and thermodynamics investigation. J Mater Chem A, 2019, 7: 17014–17021
15 Li YY, Wei ZH, Fan JB, *et al.* Photocatalytic CO_2 reduction activity of Z-scheme CdS/$CdWO_4$ catalysts constructed by surface charge directed selective deposition of CdS. Appl Surf Sci, 2019, 483: 442–452
16 Kim JH, Magesh G, Kang HJ, *et al.* Carbonate-coordinated cobalt co-catalyzed $BiVO_4$/WO_3 composite photoanode tailored for CO_2 reduction to fuels. Nano Energy, 2015, 15: 153–163
17 Di T, Xu Q, Ho WK, *et al.* Review on metal sulphide-based Z-scheme photocatalysts. ChemCatChem, 2019, 11: 1394–1411
18 Wang L, Wang Y, Cheng Y, *et al.* Hydrogen-treated mesoporous WO_3 as a reducing agent of CO_2 to fuels (CH_4 and CH_3OH) with enhanced photothermal catalytic performance. J Mater Chem A, 2016, 4: 5314–5322
19 Chen X, Zhou Y, Liu Q, *et al.* Ultrathin, single-crystal WO_3 nanosheets by two-dimensional oriented attachment toward enhanced photocatalystic reduction of CO_2 into hydrocarbon fuels under visible light. ACS Appl Mater Interfaces, 2012, 4: 3372–3377
20 Jiang L, Wang K, Wu X, *et al.* Amorphous bimetallic cobalt nickel sulfide cocatalysts for significantly boosting photocatalytic hydrogen evolution performance of graphitic carbon nitride: Efficient interfacial charge transfer. ACS Appl Mater Interfaces, 2019, 11: 26898–26908
21 Li Y, Li J, Zhang G, *et al.* Selective photocatalytic oxidation of low concentration methane over graphitic carbon nitride-decorated tungsten bronze cesium. ACS Sustain Chem Eng, 2019, 7: 4382–4389
22 Wang PQ, Bai Y, Luo PY, *et al.* Graphene-WO_3 nanobelt composite: Elevated conduction band toward photocatalytic reduction of CO_2 into hydrocarbon fuels. Catal Commun, 2013, 38: 82–85
23 Jin J, Yu J, Guo D, *et al.* A hierarchical Z-scheme CdS-WO_3 photocatalyst with enhanced CO_2 reduction activity. Small, 2015, 11: 5262–5271
24 Shi W, Guo X, Cui C, *et al.* Controllable synthesis of Cu_2O decorated WO_3 nanosheets with dominant (001) facets for photocatalytic CO_2 reduction under visible-light irradiation. Appl Catal B-Environ, 2019, 243: 236–242

25 Sun S, Watanabe M, Wu J, *et al.* Ultrathin WO_3·0.33H_2O nanotubes for CO_2 photoreduction to acetate with high selectivity. J Am Chem Soc, 2018, 140: 6474–6482
26 Li YF, Soheilnia N, Greiner M, *et al.* Pd@H_yWO_{3-x} nanowires efficiently catalyze the CO_2 heterogeneous reduction reaction with a pronounced light effect. ACS Appl Mater Interfaces, 2019, 11: 5610–5615
27 Xi G, Ouyang S, Li P, *et al.* Ultrathin $W_{18}O_{49}$ nanowires with diameters below 1 nm: Synthesis, near-infrared absorption, photoluminescence, and photochemical reduction of carbon dioxide. Angew Chem, 2012, 124: 2445–2449
28 Wang H, Zhang L, Wang K, *et al.* Enhanced photocatalytic CO_2 reduction to methane over WO_3·0.33H_2O *via* Mo doping. Appl Catal B-Environ, 2019, 243: 771–779
29 Wang L, Ha MN, Liu Z, *et al.* Mesoporous WO_3 modified by Mo for enhancing reduction of CO_2 to solar fuels under visible light and thermal conditions. Integr Ferroelect, 2016, 172: 97–108
30 Zhang N, Jalil A, Wu D, *et al.* Refining defect states in $W_{18}O_{49}$ by Mo doping: A strategy for tuning N_2 activation towards solar-driven nitrogen fixation. J Am Chem Soc, 2018, 140: 9434–9443
31 Wu X, Li Y, Zhang G, *et al.* Photocatalytic CO_2 conversion of $M_{0.33}WO_3$ directly from the air with high selectivity: Insight into full spectrum-induced reaction mechanism. J Am Chem Soc, 2019, 141: 5267–5274
32 Li Y, Wang X, Gong J, *et al.* Graphene-based nanocomposites for efficient photocatalytic hydrogen evolution: Insight into the interface toward separation of photogenerated charges. ACS Appl Mater Interfaces, 2018, 10: 43760–43767
33 Wang K, Zhang G, Li J, *et al.* 0D/2D Z-scheme heterojunctions of bismuth tantalate quantum dots/ultrathin g-C_3N_4 nanosheets for highly efficient visible light photocatalytic degradation of antibiotics. ACS Appl Mater Interfaces, 2017, 9: 43704–43715
34 Zhou L, Zhu J, Yu M, *et al.* $Mo_xW_{1-x}O_3$·0.33H_2O solid solutions with tunable band gaps. J Phys Chem C, 2010, 114: 20947–20954
35 Li Y, Wu X, Li J, *et al.* Z-scheme g-C_3N_4@Cs_xWO_3 heterostructure as smart window coating for UV isolating, Vis penetrating, NIR shielding and full spectrum photocatalytic decomposing VOCs. Appl Catal B-Environ, 2018, 229: 218–226
36 Wu X, Wang J, Zhang G, *et al.* Series of M_xWO_3/ZnO (M = K, Rb, NH_4) nanocomposites: Combination of energy saving and environmental decontamination functions. Appl Catal B-Environ, 2017, 201: 128–136
37 Yin H, Kuwahara Y, Mori K, *et al.* High-surface-area plasmonic MoO_{3-x}: Rational synthesis and enhanced ammonia borane dehydrogenation activity. J Mater Chem A, 2017, 5: 8946–8953
38 Zhang S, Shi Y, He T, *et al.* Ultrathin tungsten bronze nanowires with efficient photo-to-thermal conversion behavior. Chem Mater, 2018, 30: 8727–8731
39 Huang H, Tu S, Zeng C, *et al.* Macroscopic polarization enhancement promoting photo- and piezoelectric-induced charge separation and molecular oxygen activation. Angew Chem Int Ed, 2017, 56: 11860–11864

Acknowledgements This work was supported by the National Natural Science Foundation of China (21975193 and 51602237), and the Fundamental Research Funds for the Central Universities (195208011).

Author contributions Wu X and Wang J conceived the idea of the work. Yi L performed the preparation of materials and characterizations. Huang Y and Zhao W analyzed the photocatalytic activity. Wu X wrote the manuscript. Zhang G revised the manuscript. All authors participated in the discussion of the manuscript.

Conflict of interest The authors declare no conflict of interest.

Supplementary information Supporting data are available in the online version of the paper.

Lian Yi obtained his Bachelor's degree from East China University of Technology in 2014. Now, he studies as a master candidate at Wuhan University of Technology, and his current research focuses on nanoscale functional materials.

Xiaoyong Wu is an associate professor at Wuhan University of Technology. He obtained his BSc degree from China University of Geosciences in 2008, and PhD degree in environmental science from Tohoku University in 2015. His current research mainly focuses on nanoscale functional materials for environmental purification and energy conversion.

Jinlong Wang obtained his BSc degree from China University of Mining Technology, and PhD degree from Tsinghua University. Now, He works at Wuhan University of Technology. His current research focuses on material synthesis and applications in the field of indoor air cleaning.

钼改性的钨青铜$Cs_{0.33}WO_3$纳米棒用于增强光催化还原空气气氛中CO_2的性能

易炼, 赵文慧, 黄艳红, 吴晓勇*, 王金龙*, 张高科

摘要 光催化还原CO_2被公认为一种很有潜力缓解能源危机和环境污染的方法. 理所当然地, 改性或者开发合适的光催化材料使其拥有高的光催化CO_2还原活性成为了一个研究热点. 在本工作中, 我们用一种"控制水释放"的水热法制备了一系列钼改性的钨青铜$Cs_{0.33}WO_3$, 以期该物质能拥有良好的光催化CO_2还原性能. 有趣的是, 通过部分Mo取代晶体中的W, $Cs_{0.33}WO_3$的光催化CO_2还原性能得到显著提高, 明显优于纯的$Cs_{0.33}WO_3$和Mo掺杂的$W_{18}O_{49}$. 5%Mo掺杂的$Cs_{0.33}WO_3$在厌氧气氛中展现出了最优的光催化还原低浓度CO_2性能, 其中CO产率为7.5 μmol g^{-1} h^{-1}, 而甲醇产率为3.0 μmol g^{-1} h^{-1}. 更重要的是, Mo掺杂的$Cs_{0.33}WO_3$系列在氧气存在的条件下, 能够直接光催化还原空气气氛中的CO_2, 这有利于其实际应用. Mo掺杂的$Cs_{0.33}WO_3$光催化活性优于其他对应材料, 主要原因是Mo^{5+}的等离子共振引起的光吸收增强、大大提高的电荷分离能力以及Mo和Cs在晶体中的共同作用等. 本工作可能为设计用于高效低浓度CO_2还原的光催化材料提供一种简易的方法.

